Nonlinear Estimation of the Lateral Displacement Using Tissue Incompressibility

Andrei R. Skovoroda, Mark A. Lubinski, *Student Member, IEEE*, Stanislav Y. Emelianov, *Member, IEEE*, and Matthew O'Donnell, *Fellow, IEEE*

***Abstract*—Using the incompressibility property of soft tissue, high quality lateral displacement distributions can be reconstructed from accurate axial displacement measurements and noisy lateral displacement estimates. Previous methods appropriate for small deformations have been extended for high magnitude deformations requiring a nonlinear model. Problems arising in incompressibility processing for large deformations are considered. Applications of nonlinear incompressibility methods to ultrasonic measurements on gel-based, tissue equivalent phantoms are given. Lateral displacement images reconstructed with nonlinear methods are compared to those reconstructed with linear methods for both small and large deformations.**

I. Introduction

The ultimate goal of elasticity imaging for biomedical applications is to reconstruct the shear (or Young's) elastic modulus of soft tissue from measurements of internal mechanical deformations. For general boundary conditions, all displacement components and spatial derivatives of the displacement must be used for an accurate reconstruction even assuming a linear theory of elasticity [1]–[3]. Lateral displacement estimates are less accurate than axial, however, if ultrasound images are used for motion tracking [4]–[7]. We previously showed that the incompressibility property of soft tissue can be exploited to greatly improve the accuracy and signal-to-noise ratio (SNR) of ultrasonic lateral displacement measurements [6]. Such processing is based on a kinematical incompressibility condition and can be used for elastic, viscoelastic, or inelastic but incompressible materials. The specific methods presented in this previous work were based on a linear strain-displacement relation assuming small displacements and strains. They fail in the limit of large strains. Because large applied deformations can enhance the SNR of displacement and strain images, it is necessary to extend incompressibility methods to the high strain regime where a nonlinear representation of the strain tensor must be used. This extension is key to developing a fully nonlinear reconstruction procedure appropriate for large deformations.

In Section II, an algorithm for nonlinear lateral displacement reconstruction assuming a plane strain state is presented in detail. In the following section, this algorithm is tested using experimental displacement images of tissue equivalent, gel-based phantoms.

Manuscript received March 17, 1997; accepted October 28, 1997.

A. R. Skovoroda is with the Institute of Mathematical Problems of Biology, Russian Academy of Sciences, Pushchino, Moscow Region, Russia 142292.

M. A. Lubinski, S. Y. Emelianov, and M. O'Donnell are with the Biomedical Engineering Department, and Electrical Engineering and Computer Science Department, University of Michigan, Ann Arbor, MI 48109-2125 (e-mail: odonnel@eecs.umich.edu).

II. Theory

Consider large deformations of a constrained mechanical body such that the linear theory of elasticity is not adequate to describe internal displacements and strains. For this case, the nonlinear components of the Lagrange strain tensor in Cartesian coordinates, ε_{ij}, $i,j = 1,2,3$, take the form [8]–[11]:

$$\varepsilon_{ij} = \frac{1}{2}(u_{i,j} + u_{j,i} + \sum_k u_{k,i}u_{k,j}), \tag{1}$$

where the displacement vector is defined as $\mathbf{U} = (u_1, u_2, u_3)$, and the spatial derivatives of u_i with respect to Lagrangian coordinate x_j in the strain equation are denoted by $u_{i,j}$, i.e., $u_{i,j} = \partial u_i/\partial x_j$.

If the magnitudes of the spatial derivatives of all displacement components are small, the last nonlinear term in (1) can be omitted and the strain tensor reduces to its linear form,

$$\varepsilon_{ij}^{\text{lin}} = \frac{1}{2}(u_{i,j} + u_{j,i}). \tag{2}$$

For incompressible materials, the deformations are isochoric and must satisfy the condition [12]:

$$\det F = 1, \tag{3}$$

where F is a deformation gradient, defined as $F_{ij} = \delta_{ij} + u_{i,j}$, i.e.,

$$F = \begin{pmatrix} 1+u_{,x} & u_{,y} & u_{,z} \\ v_{,x} & 1+v_{,y} & v_{,z} \\ w_{,x} & w_{,y} & 1+w_{,z} \end{pmatrix}. \tag{4}$$

In (4), spatial coordinates x_1, x_2, and x_3 are denoted by x, y, and z. Similarly, the displacement components u_1, u_2, and u_3 are denoted by u, v, and w.

0885–3010/98$10.00 © 1998 IEEE

In the main body of the paper, we consider a plane strain state appropriate for two-dimensional ultrasound imaging. As shown previously, a plane strain state, where the out of plane displacement w is either zero or small compared to the other components, and the two in-plane components u and v do not vary significantly as functions of the out-of-plane coordinate, can be closely approximated with a simple deformational system [2], [3], [6], [13]. In the Appendix, the general three-dimensional strain state is considered.

For the plane strain case, the deformation gradient is defined as:

$$F = \begin{pmatrix} 1+u_{,x} & u_{,y} & 0 \\ v_{,x} & 1+v_{,y} & 0 \\ 0 & 0 & 1 \end{pmatrix}, \tag{5}$$

where the derivatives of the out-of-plane displacement w vanish, and only spatial derivatives of both the accurately measured axial displacement $v(x,y)$, and the less accurately estimated lateral displacement $u(x,y)$ are present.

Inserting (5) into (3), the incompressibility condition under a plane strain can be expressed as a partial differential equation,

$$u_{,x} + v_{,y} + u_{,x}v_{,y} - v_{,x}u_{,y} = 0. \tag{6}$$

Note, that if the magnitude of spatial derivatives of displacement components is small, the nonlinear terms in (6) can be omitted and the equation reduces to the linear incompressibility condition, $\nabla \cdot \mathbf{U} = u_{,x} + v_{,y} = 0$. This linear approximation has been used previously for lateral displacement estimation [6]. In the nonlinear case, however, the more complex incompressibility condition (6) contains all first spatial derivatives of displacement vector components, $u_{,x}$, $u_{,y}$, $v_{,x}$, and $v_{,y}$. Consequently, the straightforward method presented in our previous work [6] cannot be used for large deformations.

Equation (6) represents the most general form of the incompressibility condition for a plane strain state. To estimate the lateral displacement $u(x,y)$ from accurate axial displacements $v(x,y)$ using this equation, we rewrite it in a form more appropriate for numerical processing:

$$u_{,x} = (v_{,x}u_{,y} - v_{,y})/(1+v_{,y}). \tag{7}$$

Written in this way, it's clear that the incompressibility condition (7) relates the two spatial derivatives of the lateral displacement u, given that $v_{,x}(x,y)$ and $v_{,y}(x,y)$ are directly computed from accurate axial displacement measurements and, therefore, can be considered known functions. Consequently, (7) can be solved numerically over a region of interest (ROI) if the lateral displacement distribution $u(x_0,y) = u_0(y)$ is known for any single line $x = x_0$.

To solve (7), the ROI is discretized using a rectangular grid (x_i, y_j), $1 \le i \le N$, $1 \le j \le M$, and the position x_0 corresponding to $u_0(y)$ is specified along the grid at $x = x_{i_0}$. Given this formulation, (7) can be rewritten as:

$$\tilde{u}_{,x}(i,j) = \frac{v_{,x}(i,j)\tilde{u}_{,y}(i,j) - v_{,y}(i,j)}{1+v_{,y}(i,j)}, \tag{8}$$

where $\tilde{u}_{,x}(i,j)$ and $\tilde{u}_{,y}(i,j)$ are the finite difference approximations of derivatives $u_{,x}$ and $u_{,y}$ at the grid point (x_i, y_j). At $i = i_0$ the lateral displacement is $u(i_0,j) = u_0(j)$. Consequently, $\tilde{u}_{,y}(i_0,j)$ can be simply computed at each j using a finite difference form of the spatial derivative. Denoting this function as $f(j) = \tilde{u}_{,y}(i_0,j)$, (8) reduces to

$$\tilde{u}_{,x}(i_0,j) = \frac{v_{,x}(i,j)f(j) - v_{,y}(i,j)}{1+v_{,y}(i,j)}. \tag{9}$$

The displacement along lines $i = i_0 \pm 1$ can be obtained from (9) using the one-sided finite difference approximation of $\tilde{u}_{,x}(i_0,j)$,

$$u(i_0 \pm 1, j) = u_0(j) \pm h\tilde{u}_{,x}(i_0,j), \tag{10}$$

where h is a grid step in the x direction. Starting from i_0, the procedure bootstraps out to other positions (i.e., where i does not equal $i_0 \pm 1$) using the symmetric, 2nd order, finite difference approximation of $\tilde{u}_{,x}(i,j)$,

$$u(i \pm 1, j) = u(i \mp 1, j) \pm 2h\tilde{u}_{,x}(i,j). \tag{11}$$

For example, the lateral displacement at (i_0+2, j) is:

$$u(i_0+2, j) = u(i_0, j) + 2h\tilde{u}_{,x}(i_0+1, j), \tag{12}$$

where $\tilde{u}_{,x}(i_0+1,j)$ can be computed from (8) using a first order ($j = 1$ or $j = M$), or second order ($1 < j < M$), finite difference approximation of $\tilde{u}_{,y}(i_0+1,j)$ given $u(i_0+1,j)$. Therefore, the distribution $u(x,y)$ can be estimated throughout the entire ROI if the distribution $u(x_0,y) = u_0(y)$ for any line $x = x_0$ is known.

The one-dimensional distribution $u_0(y)$ can be accurately estimated from noisy measurements of the lateral displacement $u^m(x,y)$ over the ROI using a procedure similar to the least squares method described in [6]. Accordingly, the total error $\|u - u^m\|$ is minimized across the area $\mathbf{S}$ of the ROI to find the unknown function $f(j)$. Here $u(x,y)$ is the numerical solution of (8), $u^m(x,y)$ is the measured lateral displacement and $\|f\| = \left[\iint_S f(x,y)^2\, ds\right]^{1/2}$ is the norm of the function $f(x,y)$. In contrast with the linear case [6], this minimization problem has no analytical solution due to the specific form of (6). Therefore, it must be solved numerically.

For the results presented below, numerical minimization was simplified using a polynomial representation of $u_0(y)$. Because (6) is linear with respect to the unknown function $u(x,y)$, this equation was solved for a set of particular solutions of the form $u_p(x_0,y) = y^p$, $p = 1, \ldots, P$, where P is a desired order of the polynomial approximation of $u_0(y)$. Therefore, a set of particular solutions $u_p(x,y)$ of (6) was obtained. The unknown polynomial coefficients were defined by minimizing the total error $\|u - u^m\|$, where $u(x,y)$ is a linear combination of $u_p(x,y)$. The unknown polynomial coefficients were found by solving the corresponding system of linear algebraic equations. In particular, a 6th order polynomial approximation of $u_0(y)$ was used, although the final results were not sensitive to the specific order selected.

III. Experimental Methods and Materials

Experiments were performed on a pair of cylindrical, gel-based phantoms. Methods to fabricate these phantoms and to measure internal displacement and strain distributions within the phantoms due to externally applied surface deformations are detailed in previous publications [1], [2], [7]. Briefly, both phantoms were 88 mm in diameter, but one was homogeneous, and the second had a cylindrical hard inclusion with diameter of about 32 mm located near the center of the phantom. The material forming the inclusion had a Young's modulus about 2.5 times larger than that of the surrounding material. Phantoms were placed in a water tank with a 3.5 MHz, 128 channel, one-dimensional transducer array attached to the bottom, and a hydraulically driven 14 mm wide piston positioned at the top to produce incremental surface deformation of the phantom.

A large set of complex, baseband images (i.e., ultrasound images retaining phase information) were acquired during surface deformation, where consecutive measurements were separated by a piston displacement of 300 μm, and differential displacement and strain images were computed. To test the nonlinear lateral displacement reconstruction method described above for both small and high magnitude deformations, differential displacement and strain images were accumulated to produce compiled images corresponding to approximately 6.8% and 20.5% mean strain (6 mm and 18 mm total surface displacement) along the vertical central line of the phantom cross-section. In all cases presented below, the compiled images are displayed in the initial undeformed geometry of the phantoms. Finally, the ROI was chosen as a 44 mm by 44 mm square located near the center of the phantom.

IV. Results

Measured axial displacement images $v^m(x,y)$ within the 44 mm by 44 mm ROI are presented in Fig. 1. The two left panels were acquired with a 6 mm surface displacement, whereas the two right panels were acquired with an 18 mm surface displacement. Results from the homogeneous phantom are presented on the top, and results from the inhomogeneous phantom are presented on the bottom. The two left-hand panels, corresponding to the small deformation, are displayed over a dynamic range of 1.95 to 3.95 mm. Similarly, the two right-hand panels, corresponding to the large deformation, are displayed over a dynamic range of 4.5 to 12.0 mm.

The absolute value of measured $v^m_{,y}(x,y)$ distributions within the ROI are presented in Fig. 2. Again, the two left-hand panels represent the small deformation case, the two right-hand panels the large deformation case, the two top panels the homogeneous phantom, and the two lower panels the inhomogeneous phantom. The two left-hand panels are displayed over a dynamic range of 2.75% to 7.75% and the two right-hand panels are displayed over a dynamic range of 11.0% to 29.0%. The hard inclusion is clearly indicated by the dark area near the center of Figs. 2(b) and (d), similar to previously reported results [1]–[3].

Although the measured $v^m(x,y)$ and $v^m_{,y}(x,y)$ distributions of Figs. 1 and 2 exhibit reasonable contrast to noise ratio, they are still too noisy to use directly in a quantitative reconstruction of the lateral displacement. As discussed in [7], the specific method used here for strain and displacement imaging includes a spatial filter limiting the resolution of $v^m(x,y)$ and $v^m_{,y}(x,y)$ images to 2.5 to 3 mm. In addition, this same filter does not completely suppress high spatial frequency noise. Because spatial derivatives of both quantities are used for lateral displacement reconstruction, noise at high spatial frequencies, even of small magnitude, can have significant impact. To overcome this limitation, both $v^m(x,y)$ and $v^m_{,y}(x,y)$ have been spatially filtered to eliminate unwanted high frequency noise yet preserve the spatial resolution of the original displacement and strain images.

The filtering approach used here was based on a Fourier series fit to both displacement and strain images. First, a 58 mm × 58 mm region centered on the ROI was used in a least-squares fit to a K term, two-dimensional Fourier series representation of the images. For a strain image, it takes the form:

$$v^K_{,y}(x,y) = \frac{1}{2}\left[\frac{1}{2}A_{11} + \sum_{n=2}^{K_x+1} A_{1n}\cos\left(\pi(n-1)\frac{(x-x_1)}{X}\right)\right] + \sum_{k=2}^{K_y+1}\left[\frac{1}{2}A_{k1} + \sum_{n=2}^{K_x+1} A_{kn}\cos\left(\pi(n-1)\frac{(x-x_1)}{X}\right)\right]\times \cos\left(\pi(k-1)\frac{(y-y_1)}{Y}\right), \quad (13)$$

where $X = x_N - x_1$ and $Y = y_M - y_1$ are the dimensions of the ROI, $K = K_x = K_y$ is the order of the fit, and A_{kn} are Fourier coefficients. A similar fit was performed for $v^K(x,y)$. The term $v^K_{,x}(x,y)$ was obtained by differentiating $v^K(x,y)$ along the x direction.

Because the spatial resolution of the strain images is about 2.5 to 3 mm, the Fourier series was terminated at 19 terms (i.e., $K = 19$). The resultant Fourier coefficients from the fit produced filtered displacement and strain images over the 44 mm × 44 mm ROI. The larger 58 mm × 58 mm region was used for the fit to eliminate boundary effects on this Fourier approximation within the ROI. Filtered $v^m(x,y)$ and $v^m_{,y}(x,y)$ distributions corresponding to the same data as Figs. 1 and 2 are shown in Figs. 3 and 4. Precisely the same display format and dynamic range are used for these images.

Measured lateral displacement images $u^m(x,y)$ within the ROI are presented in Fig. 5. Once again, the two left panels represent the small deformation case, the two right panels the large deformation case, the two top panels the homogeneous phantom, and the two lower panels the inhomogeneous phantom. The two left panels are displayed over a dynamic range of ±1 mm, where black represents

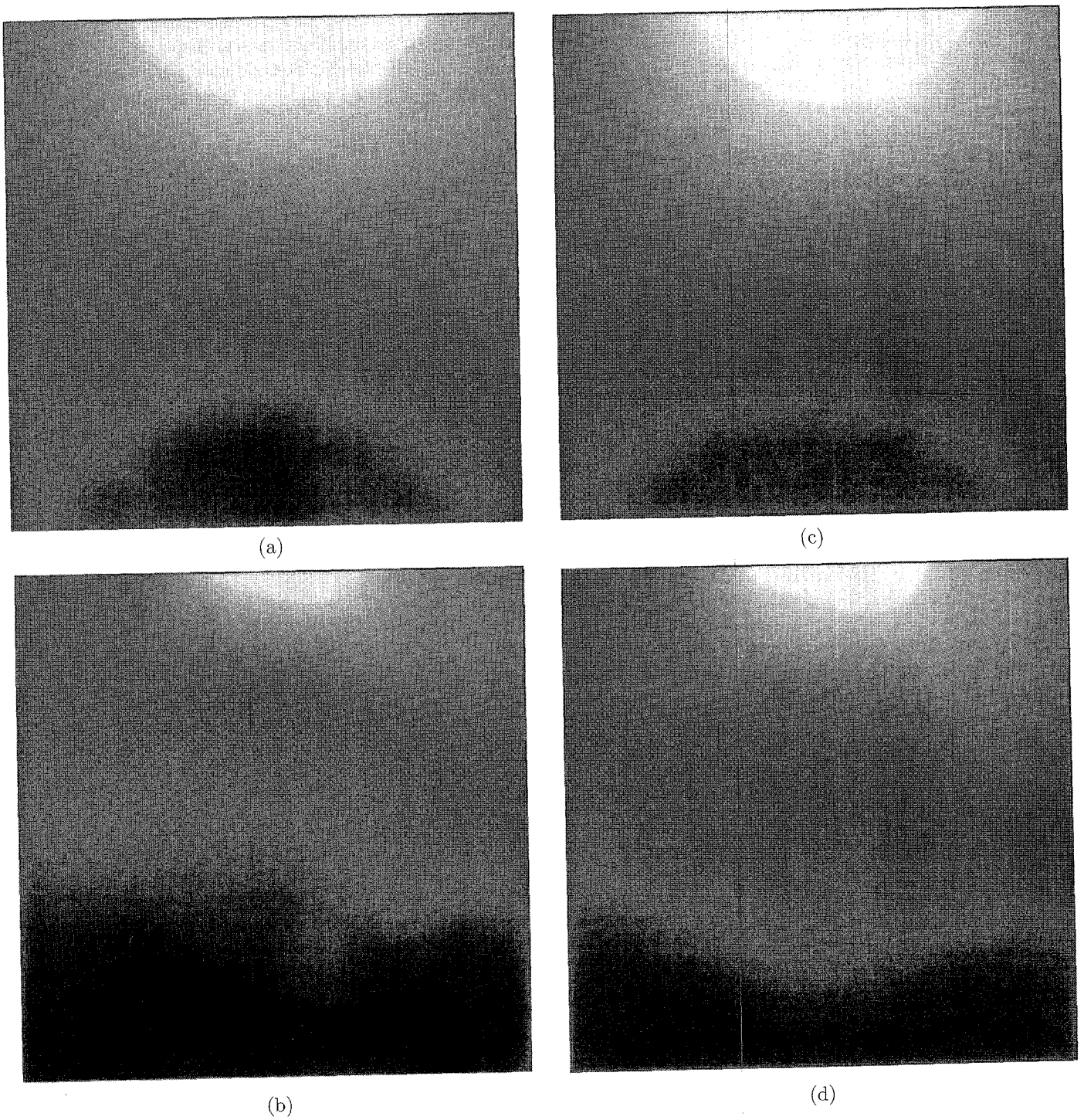

Fig. 1. Measured axial displacement, $v^m(x, y)$, images in a 44 mm $\times$ 44 mm region of interest. The left two panels (a, b) were produced with small surface deformations and the right two panels (c, d) were produced with large surface deformations. The top two panels (a, c) correspond to the homogeneous phantom, and the bottom two panels (b, d) correspond to the phantom with a single hard inclusion at the center.

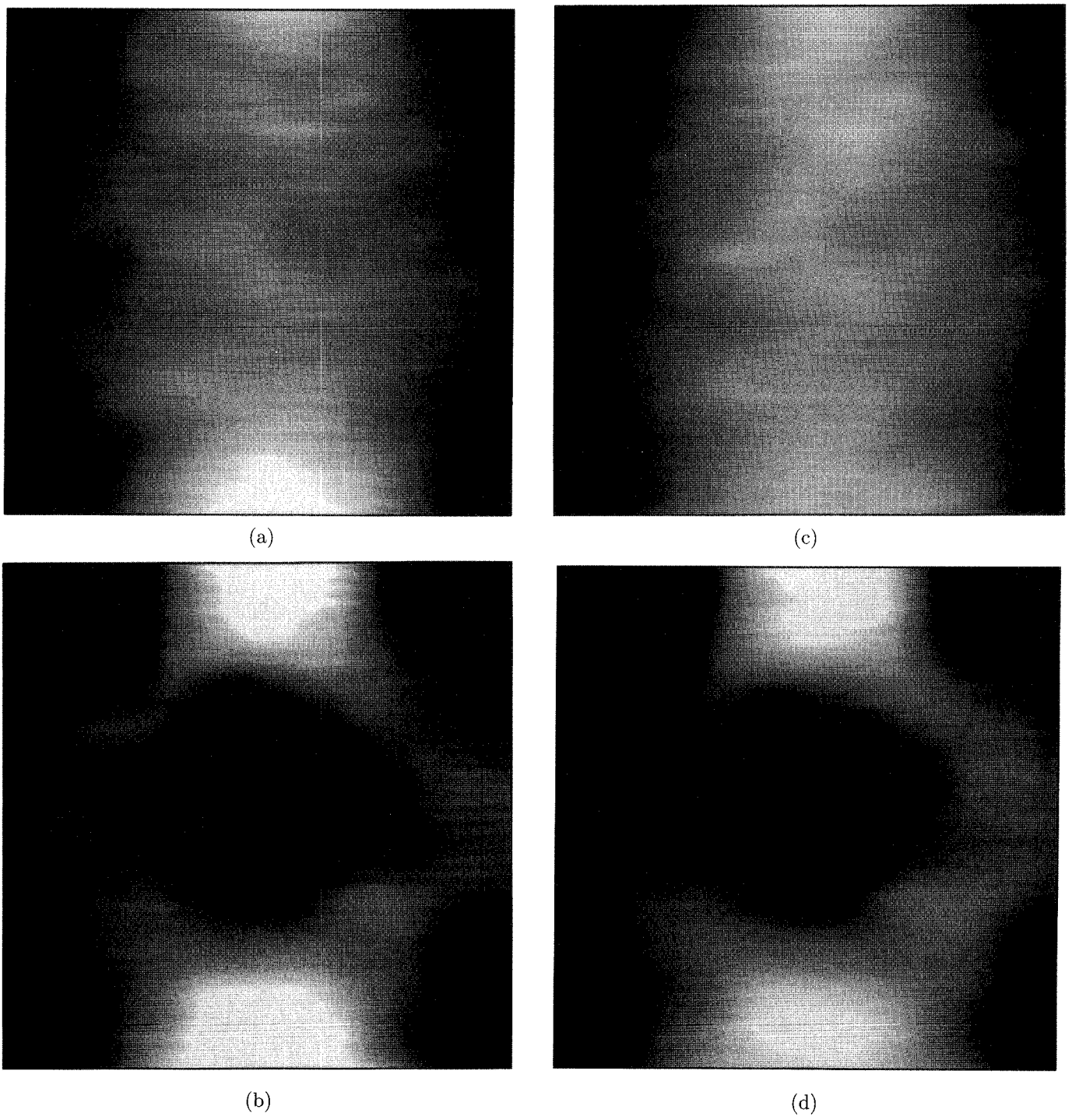

Fig. 2. Measured normal, axial strain, $v^m_{,y}(x, y)$, images for the same cases presented in Fig. 1.

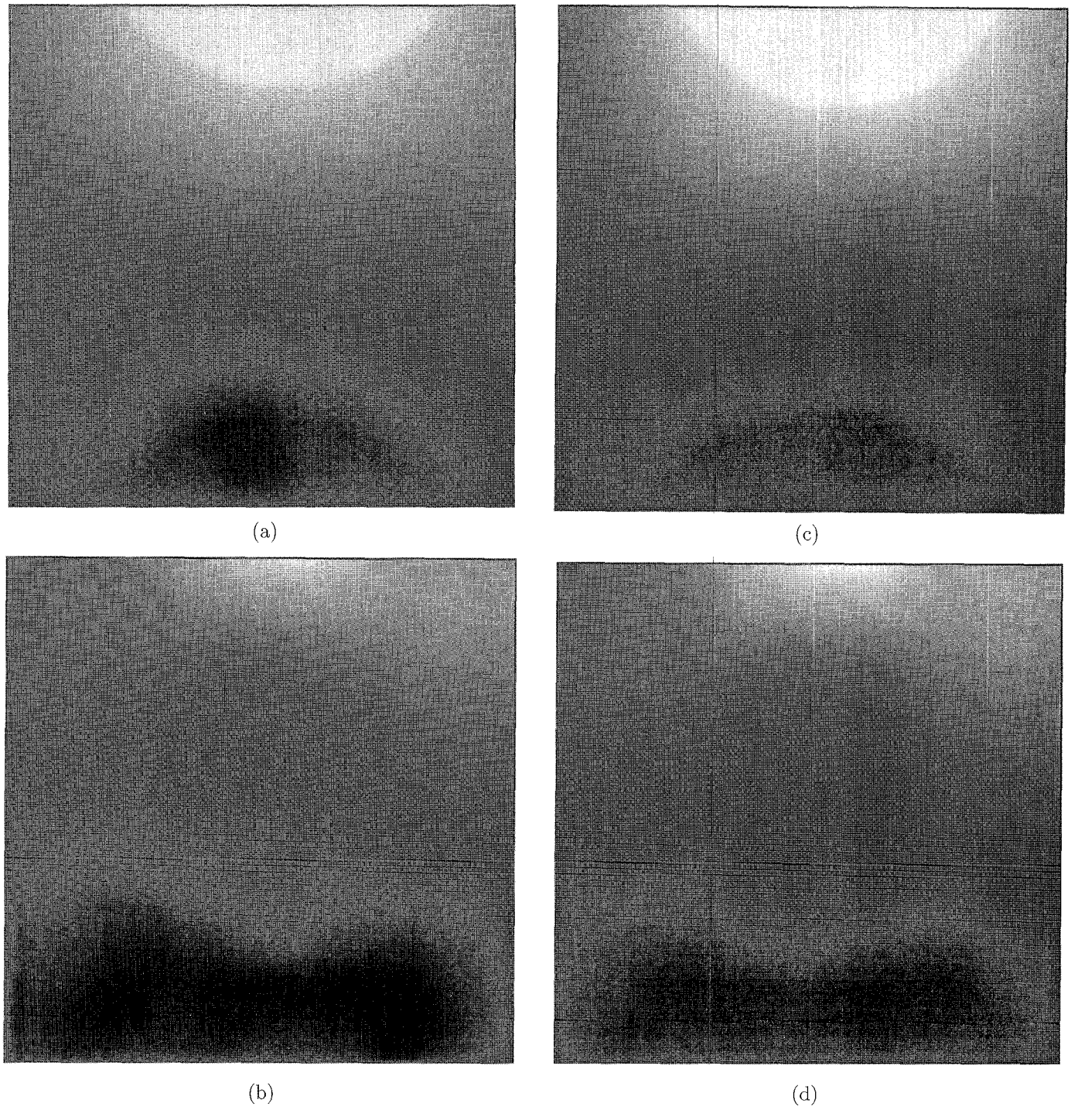

Fig. 3. Fourier filtered images of the axial displacement distributions of Fig. 1.

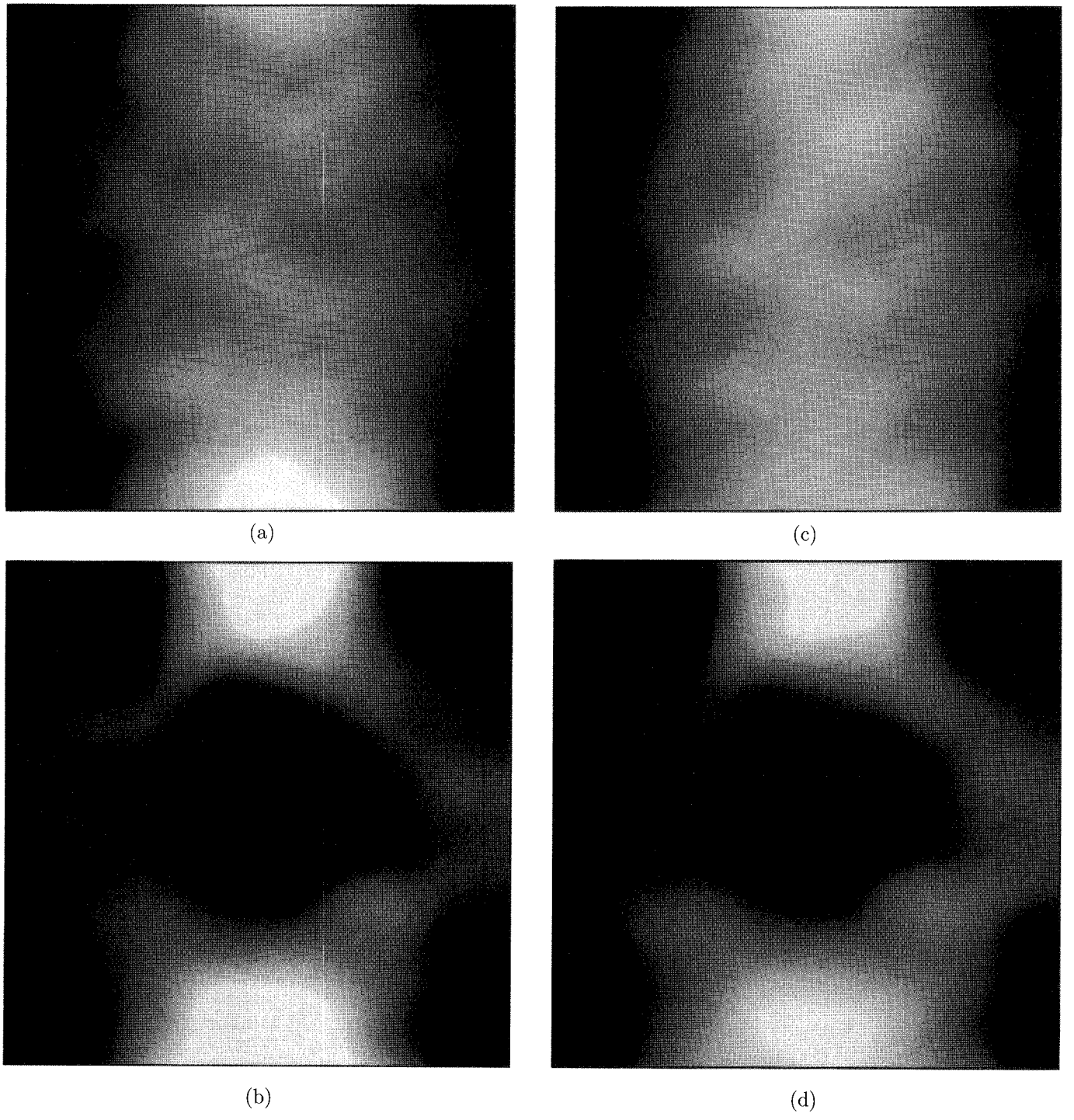

Fig. 4. Fourier filtered images of the normal, axial strain distributions of Fig. 2.

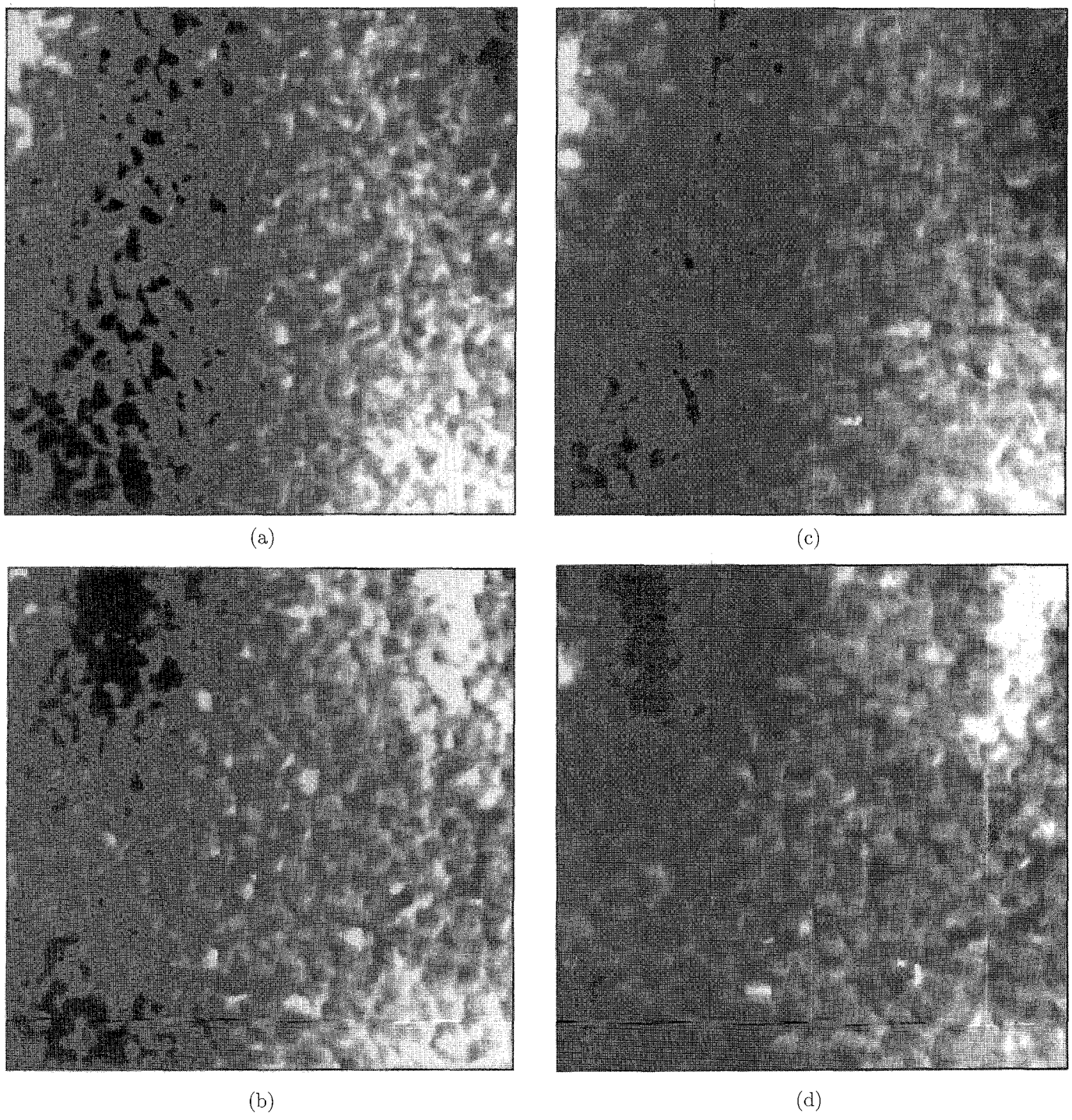

Fig. 5. Measured lateral displacement, $u^m(x, y)$, images for the same cases presented in Fig. 1.

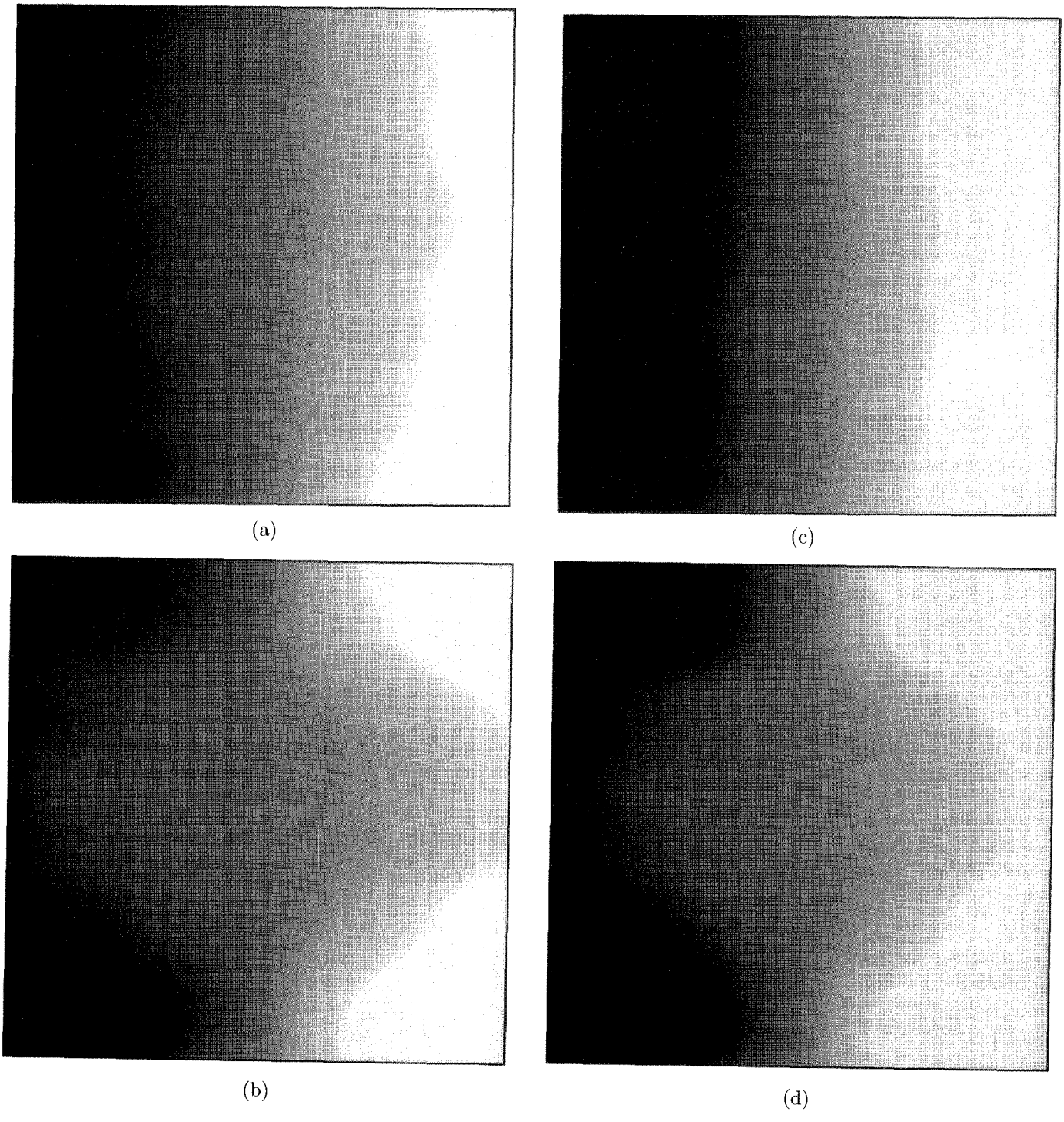

Fig. 6. Reconstructed lateral displacement images for the same cases presented in Fig. 1.

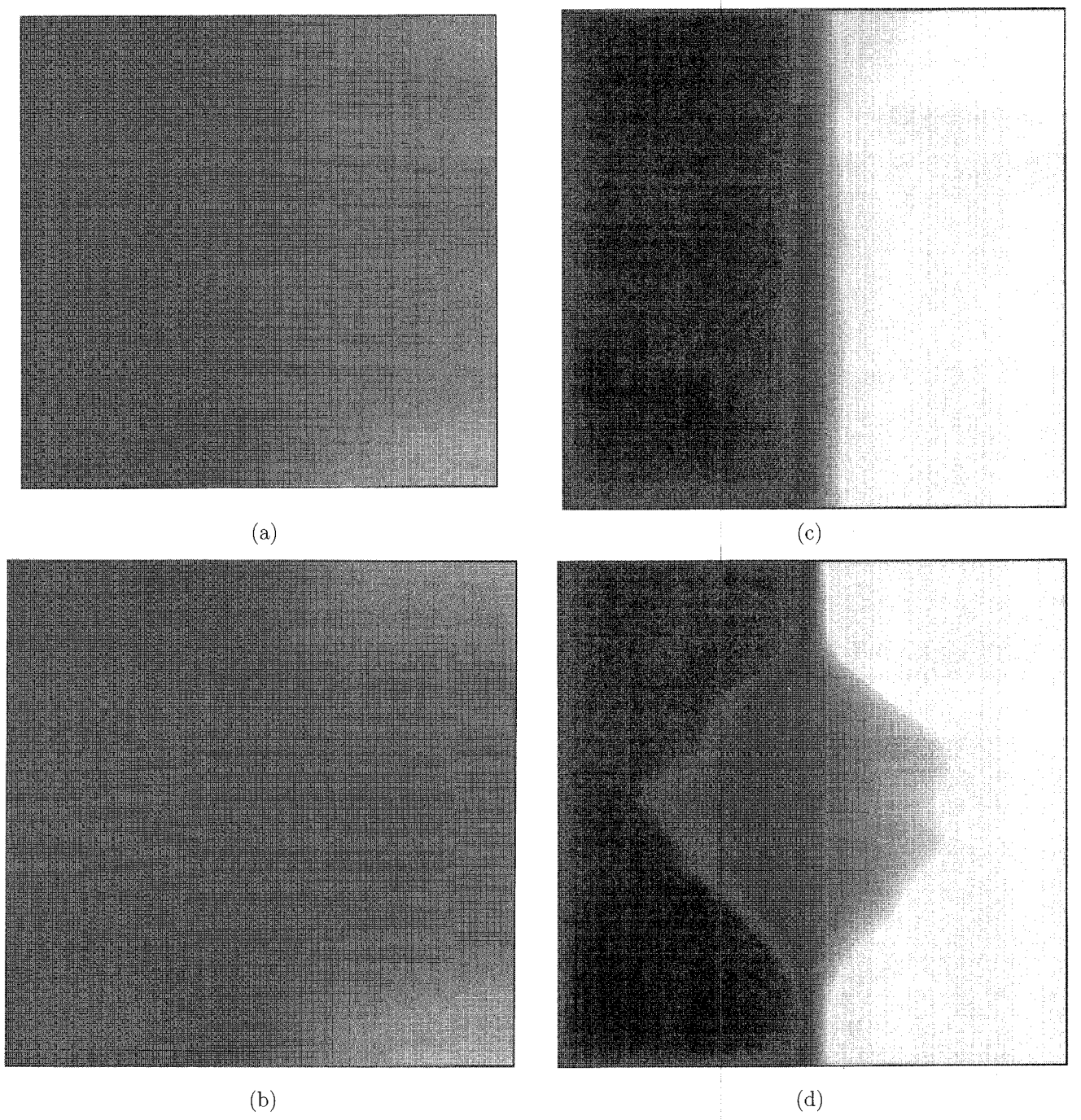

Fig. 7. Difference between linear and nonlinear reconstructions of the lateral displacement, $\Delta u = u^{\text{lin}} - u^{\text{nonlin}}$, for the same cases presented in Fig. 1.

motion to the left (i.e., negative lateral displacement) and white represents motion to the right (i.e., positive lateral displacement), and the right panels are displayed over a dynamic range of ±3.5 mm. There are significant artifacts in these images due to imperfect beam forming in the synthetic aperture system used for data acquisition [6]. Because of the poor contrast to noise ratio in these images, the hard inclusion is difficult to identify.

Images of the lateral displacement $u(x, y)$ within the ROI reconstructed by (8) are presented in Fig. 6. These reconstructions used the filtered versions of $v^m(x, y)$ and $v^m_{,y}(x, y)$ presented in Figs. 3 and 4. The display format and dynamic range of Fig. 6 are identical to those used in Fig. 5. Variations in the lateral displacement are now clearly seen in the lower two panels around the region of the hard inclusion.

Fig. 7 presents the difference between linear and nonlinear reconstructions of the lateral displacement, $\Delta u = u^{\text{lin}} - u^{\text{nonlin}}$, where u^{lin} is estimated by the linear approach of [6], and u^{nonlin} is estimated by the nonlinear approach

TABLE I
COMPARISON OF LINEAR AND NONLINEAR RECONSTRUCTION OF THE LATERAL DISPLACEMENT.

Surface/piston displacement	6 mm		18 mm	
Phantom	Homogeneous	Inhomogeneous	Homogeneous	Inhomogeneous
$\|u^{\text{lin}} - u^{\text{nonlin}}\|/\|u^{\text{lin}}\|$	0.059 (0.073)	0.067	0.256 (0.257)	0.280

presented in this paper (Fig. 6). Once again, the two left panels represent the small deformation case, the two right panels the large deformation case, the two top panels the homogeneous phantom, and the two lower panels the inhomogeneous phantom. All images are displayed over the same dynamic range of ±0.2 mm. Clearly, the difference between linear and nonlinear reconstructions is larger for the large deformation.

The qualitative differences presented in Fig. 7 are quantitated in Table I, where the relative difference between linear and nonlinear reconstructions averaged over the entire ROI are presented. For the homogeneous case, the same computation was made using analytic expressions for the internal displacement and strain in both linear and nonlinear cases. The homogeneous rectangle was deformed between two parallel rigid plates with slippage allowed on the boundaries of the object and the plates. For the linear case, it can be easily shown that the lateral displacement reduces to the expression:

$$u = \frac{V_0}{H}x, \tag{14}$$

where H is the height of the rectangle, and V_0 is the surface displacement of the plate.

For the nonlinear case, it can be easily shown that the lateral displacement reduces to the expression:

$$u = \frac{V_0}{H - V_0}x. \tag{15}$$

Based on these analytic results, the expected relative difference between linear and nonlinear values is presented in parenthesis. Clearly, measurements parallel expected results.

Based on these results, and the images of Fig. 7, it's quite clear that both absolute and relative differences are most pronounced for the large deformation case. Consequently, nonlinear methods must be used to accurately reconstruct the lateral displacement using the incompressibility property of soft tissue if large deformations are applied.

Also, note that the influence of nonlinearities can be different within an inhomogeneous object. Figs. 7(c) and (d) illustrate this effect. In the area of the hard inclusion the magnitude of Δu is comparatively smaller because the flexibility of the inclusion is smaller than that of surrounding material, and therefore, the magnitude of spatial derivatives of the displacement is reduced. For the case of softer inclusions compared to the background, the strain can be amplified, thus heightening the influence of nonlinearities.

V. Discussion

If deformations, and corresponding internal strains, are significant, then a nonlinear mechanical model must be used. As demonstrated here, the effect of nonlinearities can be included in a more general form of incompressibility processing to produce lateral displacement images from noisy lateral displacement estimates and high quality measurements of the axial displacement. Comparison of measured and reconstructed lateral displacement distributions clearly shows that incompressibility processing greatly improves the accuracy and SNR for both linear and nonlinear cases.

Given accurate axial and lateral displacement distributions, we have demonstrated previously that high quality elasticity reconstructions can be performed using a linear mechanical model [3]. Based on the nonlinear incompressibility processing methods detailed in this paper, future work will focus on developing a fully nonlinear elasticity reconstruction approach appropriate for the case of large deformations.

Appendix

Assume that displacement components $v(x, y, z)$ and $w(x, y, z)$ are accurately measured within the volume and displacement component $u(x, y, z)$ can be estimated less accurately, as occurs, for example, in elasticity measurements using NMR [14], [15]. For this three-dimensional strain state, the general incompressibility condition (3) can be written in a form of the partial differential equation incorporating (4) into (3):

$$(u_{,x} + v_{,y} + w_{,z}) + \det\begin{pmatrix} u_{,x} & u_{,y} \\ v_{,x} & v_{,y} \end{pmatrix} + \det\begin{pmatrix} v_{,y} & v_{,z} \\ w_{,y} & w_{,z} \end{pmatrix} + \det\begin{pmatrix} u_{,x} & u_{,z} \\ w_{,x} & w_{,z} \end{pmatrix} + \det\begin{pmatrix} u_{,x} & u_{,y} & u_{,z} \\ v_{,x} & v_{,y} & v_{,z} \\ w_{,x} & w_{,y} & w_{,z} \end{pmatrix} = 0. \tag{A1}$$

Note again, that if the magnitudes of spatial derivatives of the displacement components are small, the nonlinear terms in (A1) can be omitted, and (A1) reduces to the linear incompressibility condition $\nabla \cdot \mathbf{U} = u_{,x} + v_{,y} + w_{,z} = 0$.

$$u_{,x} = \frac{(v_{,x} + v_{,x}w_{,z} - v_{,z}w_{,x})u_{,y} + (w_{,x} + v_{,y}w_{,x} - v_{,x}w_{,y})u_{,z} + (v_{,z}w_{,y} - v_{,y}w_{,z}) - v_{,y} - w_{,z}}{1 + (v_{,y} + w_{,z}) + (v_{,y}w_{,z} - v_{,z}w_{,y})}. \tag{A2}$$

To estimate $u(x, y, z)$ for the full nonlinear case, (A1) can be shown in (A2) at the top of this page. This equation also can be solved numerically in the three-dimensional region of interest if the distribution $u(x_0, y, z) = u_0(y, z)$ is known for any plane $x = x_0$. For this purpose, the ROI can be covered by a three-dimensional grid (x_i, y_j, z_k), $1 \le i \le N$, $1 \le j \le M$, $1 \le k \le K$, $x_0 = x_{i0}$, and a finite difference approximation of derivatives $u_{,x}$ and $u_{,y}$, and $u_{,z}$ at all grid points (x_i, y_j, z_k) should be used, as done above for a plane strain state. Note here that all formulas presented in this appendix reduce to the corresponding formulas of Section II under the restriction of a plane strain state.

Again, the unknown function $u_0(y, z)$ can be found by minimizing the total squared error $Q(u, u^m)$ across the volume $\mathbf{V}$ of the ROI, where $u(x, y, z)$ is the numerical reconstruction of the noisy measured displacement component, $u^m(x, y, z)$, and $Q(u, u^m) = \iiint_V (u - u^m)^2\, dV$.

References

[1] M. O'Donnell, S. Y. Emelianov, A. R. Skovoroda, M. A. Lubinski, W. F. Weitzel, and R. C. Wiggins, "Quantitative elasticity imaging," *Proc. IEEE Ultrason. Symp.*, 1993, pp. 893–903.

[2] A. R. Skovoroda, S. Y. Emelianov, M. A. Lubinski, A. P. Sarvazyan, and M. O'Donnell, "Theoretical analysis and verification of ultrasound displacement and strain imaging," *IEEE Trans. Ultrason., Ferroelect., Freq. Contr.*, vol. 41, pp. 302–313, May 1994.

[3] A. R. Skovoroda, S. Y. Emelianov, and M. O'Donnell, "Tissue elasticity reconstruction based on ultrasonic displacement and strain images," *IEEE Trans. Ultrason., Ferroelect., Freq. Contr.*, vol. 42, pp. 747–765, July 1995.

[4] I. A. Hein and W. D. O'Brien, "Current time-domain methods for assessing tissue motion by analysis from reflected echoes—A review," *IEEE Trans. Ultrason., Ferroelect., Freq. Contr.*, vol. 40, pp. 84–102, Mar. 1993.

[5] L. N. Bohs and G. E. Trahey, "A novel method for angle independent imaging of blood flow and tissue motion," *IEEE Trans. Ultrason., Ferroelect., Freq. Contr.*, vol. 38, pp. 280–286, Mar. 1991.

[6] M. A. Lubinski, S. Y. Emelianov, K. R. Raghavan, A. E. Yagle, A. R. Skovoroda, and M. O'Donnell, "Lateral displacement estimation using tissue incompressibility," *IEEE Trans. Ultrason., Ferroelect., Freq. Contr.*, vol. 43, pp. 247–256, Mar. 1996.

[7] M. O'Donnell, A. R. Skovoroda, B. M. Shapo, and S. Y. Emelianov, "Internal displacement and strain imaging using ultrasonic speckle tracking," *IEEE Trans. Ultrason., Ferroelect., Freq. Contr.*, vol. 41, pp. 314–325, May 1994.

[8] L. D. Landau and E. M. Lifshitz, *Theory of Elasticity.* Moscow: Nauka, 1965.

[9] A. A. Ilyushin, *Mechanics of Solid Structures.* Moscow: Moscow State University Press, 1978.

[10] Y. N. Rabotnov, *Mechanics of Solid Structures.* Moscow: Nauka, 1979.

[11] A. E. Green and J. E. Adkins, *Large Elastic Deformations and Non-linear Continuum Mechanics.* Oxford: Clarendon Press, 1960, pp. 2–5.

[12] M. E. Gurtin, *An Introduction to Continuum Mechanics.* New York: Academic, 1981, pp. 42, 51, 54.

[13] S. Timoshenko and J. Goodier, *Theory of Elasticity.* New York: McGraw-Hill, 1951.

[14] T. L. Chenevert, S. Y. Emelianov, and A. R. Skovoroda, "Elasticity reconstructive imaging using static displacement and strain estimations," *Proc. Int. Soc. Magnetic Resonance in Med.*, 1997, p. 461.

[15] T. L. Chenevert, A. R. Skovoroda, M. O'Donnell, and S. Y. Emelianov, "Elasticity reconstructive imaging via stimulated echo MRI," *Magnetic Resonance in Medicine*, in print, 1998.

Andrei R. Skovoroda received the B.S. and M.S. degrees in mathematics and mechanics in 1973 and 1975, respectively, from the Novosibirsk State University, USSR, and the Ph.D. degree in 1985 from the Moscow State University, USSR.

From 1975 to 1977 he was a lecturer in theoretical mechanics at the College of Textile Technology, Barnaul, USSR. From 1977 to 1980 he was a Ph.D. researcher at the subfaculty of Plasticity of the Moscow State University, where he worked on the dynamic behavior of plates under blast-type loading. In 1981 he held an appointment as a junior research associate at the Laboratory of Mathematical Modeling of the Research Computing Center of the USSR Academy of Sciences (the present name: Institute of Mathematical Problems of Biology, Russian Academy of Sciences), where he developed efficient mathematical methods to solve the differential equations of the theory of elasticity. In 1986 he became a senior research associate and was scientific secretary at the same institute from 1988 to 1993. He is currently head of the Laboratory of Mathematical Problems in Biomechanics and works on the biomechanics of soft tissue.

Dr. Skovoroda has authored and co-authored more than 80 articles for archival publications and papers presented at all-union and international meetings.

Mark A. Lubinski (S'94) received the B.S. degree in electrical engineering (with biomedical engineering option) in 1990 from Carnegie Mellon University and the M.S. in bioengineering and electrical engineering (systems) in 1993 and 1994, respectively, from the University of Michigan, Ann Arbor.

Before beginning his graduate work, he worked as a computer engineer in the Department of Neurophysiology at the Children's Hospital of Pittsburgh. While at the University of Michigan he was a National Science Foundation Graduate Fellow in Bioengineering and a GAANN Fellow. He is currently a graduate student research assistant at the University of Michigan, working in the Biomedical Ultrasonics Laboratory, pursuing a Ph.D. in biomedical engineering, and researching ultrasonic elasticity imaging. He is a member of Tau Beta Pi and Eta Kappa Nu. His research interests include signal processing, medical imaging, and motion estimation.

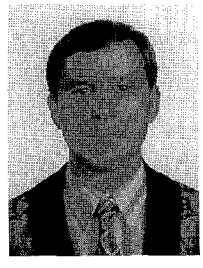

Stanislav Emelianov (M'94) was born in May 1966. He received the B.S. and M.S. degrees in physics in 1986 and 1989, respectively, from Moscow State University, and the Institute of Mathematical Problems of Biology of the Russian Academy of Sciences, Russia.

In 1989, he joined the Institute of Mathematical Problems of Biology, where he was engaged in both mathematical modeling of soft tissue biomechanics and experimental studies of noninvasive methods in medical diagnostics

based on tissue elasticity variations. Following his graduate work, he moved to the University of Michigan, Ann Arbor, as a post-doctoral *fellow* in the Electrical Engineering and Computer Science Department working on applications of imaging systems for medical diagnosis and nondestructive testing. Dr. Emelianov is currently a research scientist in the Biomedical Ultrasonics Laboratory at the University of Michigan and involved primarily in the theoretical and practical aspects of ultrasound elasticity imaging. He is the author of several scientific papers. His research interests are in the areas of tissue biomechanics, medical imaging systems, and nondestructive material testing.

Matthew O'Donnell (M'79–SM'84–F'93) received the B.S. and Ph.D. degrees in physics from the University of Notre Dame, Notre Dame, IN, 1972 and 1976, respectively.

Following his graduate work, he moved to Washington University in St. Louis as a postdoctoral fellow in the Physics Department working on applications of ultrasonics to medicine and non-destructive testing. He subsequently held a joint appointment as a Senior Research Associate in the Physics Department and a Research Instructor of Medicine in the Department of Medicine at Washington University. In 1980 he moved to General Electric Corporate Research and Development in Schenectady, New York, where he continued to work on medical electronics, including NMR and ultrasound imaging systems. During the 1984–1985 academic year, he was a visiting fellow in the Department of Electrical Engineering at Yale University investigating automated image analysis systems. Most recently, he has worked on the application of advanced VLSI circuits to medical imaging systems, including catheter arrays. In a bold move during 1990, Dr. O'Donnell moved to the Electrical Engineering & Computer Science Department at the University of Michigan in Ann Arbor, Michigan, where he is currently a Professor.

Dr. O'Donnell is a member of Sigma Xi, the American Physical Society, and is a fellow of both the IEEE and the AIMBE. He has authored or coauthored over 100 archival publications, including 2 receiving best paper awards, numerous presentations at national meetings, and 40 patents.